TUFTS UNIVERSITY

Exploring the Low and High Mass Extremes in the Distant Universe

by

Adina Feinstein

in the

Department of Physics and Astronomy

May 2018

Abstract

By studying galaxies at different redshifts, .i.e. periods of cosmic time, astronomers can combine observations and simulations to piece together the whole story. Because it is easier to find more massive, brighter sources farther away, there is an inherent bias in our observations. The *Hubble* Space Telescope combined with the gravitational lensing power of six massive galaxy clusters, known as the *Hubble* Frontier Fields (*HFF*) Campaign, has been able to uncover the faintest and least massive known galaxies at great distances. The work I present here calculates and corrects for the lensing magnifications for sources observed in the *HFF* catalogs. Additionally, I will examine the most massive ($M_*[M_\odot] \geq 10^{11}$) galaxies at $2 \leq z \leq 6$ from the extensive, multi-wavelength UltraVISTA survey. By studying both the lowest and highest mass objects in the distant universe, we can further study galaxy evolution as a function of galactic mass.

Acknowledgements

I would like to acknowledge all of the support I received from my advisor, Professor Danilo Marchesini, and from members of his research group, specifically Dr. Heath Shipley. Dr. Shipley's patience and guidance since the beginning of my research project at Tufts has been crucial to my success.

I want to acknowledge the members of my thesis committee, Professor Marchesini and Professor Anna Sajina, for both taking the time to read and support this project as well as being amazing professors for all of the astronomy courses I have taken while at Tufts.

I would also like to thank my parents for their support throughout my entire undergraduate career as I pursued my true passion. They stood by me through ups and downs and I am eternally grateful. I would like to especially thank my mom for shipping me stress-relieving cookies when needed.

Contents

List of Figures

List of Tables

Chapter 1

Introduction

When Edwin Hubble first declared that Andromeda was not part of the Milky Way, but was in fact another galaxy located entirely outside of our own, has opened up the study of galaxy formation and evolution. A galaxy, a dynamically bound system of $10^{10}+$ stars, is a physical object larger than anything the human mind can comprehend and exists at scales that far outlive human beings. Then, how can one study an object that far exceeds our own lifetimes? Light. The speed of light is finite, which means any light we receive from distant galaxies is essentially looking at said galaxy when it was younger. Thus, astronomers aim to understand how galaxies form and evolve by obtaining snapshots in time of galaxy populations and their properties and by connecting these data sets, we can obtain a more complete picture of the process.

1.1 Galaxy Evolution

The challege of studying galaxy evolution, besides the long timescales, is the diversity of the known populations. Diversity is defined by a long list of observational properties of a galaxy [4]. Some of the easiest to observe and measure are:

1. **Morphology:** There exists two dominant galactic shapes: spirals and ellipticals. Spiral galaxies are rotationally supported flat disks. There are 2 subspecies of spiral galaxies as well: flocculent, which does not have distinct arms (1.1A), and grand design, which do (1.1B). Elliptical galaxies are dispersion supported, due to the random motion of the stellar population and are not flat disk-like structures (1.1C).

2. **Stellar Mass:** The stellar mass determines the total luminosity of a galaxy, as it is dependent on the total number of stars as well as the age of the population. There

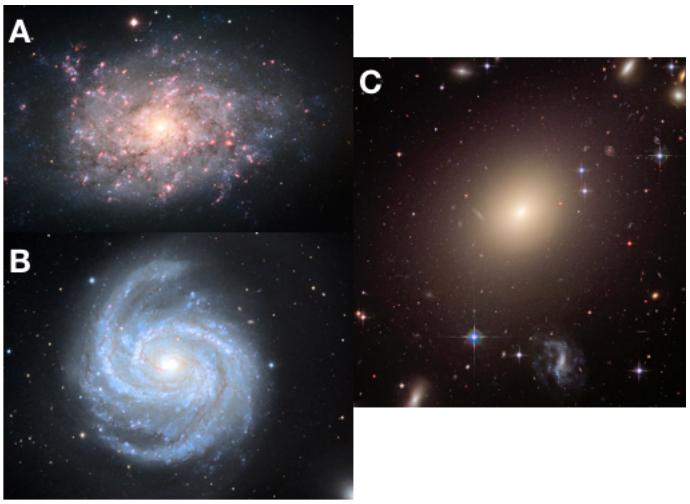

FIGURE 1.1: A comparison of the 3 main galactic morphologies: flocculent spirals (A), grand design spirals (B), and ellipticals (C). The examples provided here are NGC 7739, Messier 100, and ESO 325-G004 respectively.

is significant scatter when studying the luminosity vs. stellar mass of a galaxy due to different stellar populations. Young galaxies and star-forming galaxies are more luminous than non star-forming and older galaxies because young star-formation produces very bright, hot, and massive stars whereas non-star-forming (quiescent), old galaxies are dominated by low-mass, cooler stars. However this does not necessarily indicate that the young galaxies are more massive. The stellar population can be further probed by observing the color of the galaxy.

3. **Color:** Local galaxies grow a bimodality in optical red and blue colors. Typically, elliptical galaxies tend to be redder than spiral galaxies. The color tells the observer a significant amount about the stellar population within the galaxy as it follows stellar evolution. A star is born within a giant molecular cloud and over a few million years, evolves onto the main sequence (MS; a tight relation between the luminosity (L) and surface temperature (T_{eff}) of stars) at a location (in $L - T_{eff}$ space) set by the stellar mass. It will stay there for most of its life as it fuses hydrogen into helium. Once the hydrogen core is depleted, it will evolve off the MS. The largest stars along the MS are O dwarfs, which are very massive, hot, and blue stars with very short lifetimes (for a star). The smallest stars along the MS are M dwarfs, which are about 10% the mass of our Sun, are cold, red, and essentially live forever. With that in mind, one can make the connection that if a galaxy is bluer, there must still be the largest stars present and thus, because these stars have not left the MS, the galaxy is young. Consequently, if a galaxy appears red, then more massive, shorter lived stars have left the MS and the stellar population

that is left consists of lower mass MS stars as well as the red giant remains of the largest, blue stars, assuming no dust.

4. **Size:** Size is a hard galactic property to measure as galaxies do not have hard boundaries, but tend to taper off at the edges. Therefore, it is common practice to understand the size of the galaxy to be the radius at which half of the total luminosity is enclosed. Although it might be easy to convince oneself that brighter galaxies have larger radii, one must remember that the distribution of the luminosity within a galaxy differs from source to source and thus, a more dispersed galaxy will be larger than a bright, but condensed, galaxy.

5. **Gas Mass Fraction:** The gas mass compared to the sum of the gas mass and stellar mass allows for an analysis of the efficiency with which cold gas is being turned into stars. This property mainly applies to spirals, as they are more likely to be star-forming, than ellipticals.

6. **Environment:** Galaxies are not randomly distributed throughout the universe. Some are located in groups, like the Milky Way, consisting of two massive galaxies and several satellite galaxies, while others form in high density clusters. High density clusters of galaxies, consisting of hundreds of galaxies, play a crucial role in studying the distant universe. This will be further discussed in Section 1.2.

Of course the items listed above just begin to touch upon the diversity of galaxies in the universe. And because there is such a diverse population, the models of galaxy evolution are not easily theorized and created.

Before talking about galaxy evolution, we must discuss galaxy formation. Originally, the Eggen, Lynden-Bell Sandage collapse model (ELS collapse model) was hypothesized. The model, based on the observed correlations between stellar metallicity and orbital eccentricities suggest that, in the case of the Milky Way, galaxies form from a rapid collapse of a large proto-galatic nebula. The location of the nebula would follow the large scale dark matter structure of the Universe. The gas used to form stars within a galaxy would funnel towards the center of the structure. Along the collapse timescale, stars will form and die, enriching the environment with metals. Because most of the gas is at the center of the structure, more star formation could occur at this location, where the environment would have been enriched with metals from dead stars as well. This model follows the observed metal-poor stars that are in the halo of the galaxy, while the metal-rich stars reside in the disk. However, this model does not explain why stars and clusters in the halo are in retrograde motion and does not explain why different components of the galaxy (bulge, disk, halo) have different ages.

In order to further comprehend galaxy formation, and fix current flaws in the ELS collapse model, a hierarchical process of mergers should be included. This hierarchical model would cause collisions and tidal interactions between several pre-formed galaxies. The disruption of each galaxy involved in the merger could explain the distribution and age of the objects in the halo. This is because most of the gas would be funneled to the center of the newly merged system and thus would lead to more star formation in the central bulge.

Galaxy interactions are not only essential for formation, but also for evolution. Galaxy interactions can lead to the scattering of stellar populations, as mentioned previously. However, mergers also help reshape and increase the size of galaxies. There are types of mergers: minor and major. Minor mergers result in the cannibalization of smaller, satellite galaxies by large galaxies, while major mergers are the interaction between two galaxies of the same scale.

These properties hold true for galaxies at all epochs. The simplest way to analyze the intrinsic properties of a galaxy at high redshifts is through its colors, as mentioned when discussing the diversity in the population of galaxies. The adopted method for determining whether a galaxy is quiescent, meaning there is little to no star formation occurring, dusty star forming, meaning the galaxy is forming stars and the galaxy appears very dusty (i.e. redder), or non-dusty star forming, meaning the galaxy is forming stars and is not being obscured by dust, is through a UVJ diagram. A UVJ diagram uses the filters in the rest-frame U-band (365nm), V-band (551nm), and J-band (1220nm) to analyze the color of the galaxy. EAZY, The definition of color is

$$X - Y = -2.5log_{10}\frac{f_x}{f_y} \tag{1.1}$$

where X and Y are the bands in question and b_x and b_y are the fluxes for the X and Y bands. The UVJ diagram compares the U-V and V-J rest-frame colors to broadly characterize galaxy properties by separating the galaxy population into quiescent, unobscured star-forming, and dust-obscured star-forming galaxies.

1.2 Gravitational Lensing

As briefly mentioned in Section 1.1, there are many different environments which a galaxy can reside in. Examples include our own local neighborhood, with two major and several satellite galaxies or high density clusters. The definition of a galaxy cluster was set by Abell in 1958. The cluster criteria are as follows:

1. **Richness:** A high density cluster must contain a minimum of fifty members that are no more than 2 magnitudes fainter than the apparent magnitude of the third brightest member. Rich clusters contain > 50 members while poor clusters had 30-50 members.

2. **Compactness:** All members of the rich clusters must fall within the Abell radius, $1.5h^{-1}$Mpc where $h = H_0/100$km s^{-1} Mpc^{-1} and H_0 is Hubble's Constant.

3. **Distance:** Because Abell's work was completed using glass plates, he set a distance limit for the images on the plate itself. No cluster could extend over several plates and this was translated to a distance of 33-330 Mpc.

4. **Galactic-latitude:** Due to the high density of stars in the Milky Way, clusters at low galactic latitudes could not be completely identified. As such, those areas of the sky were excluded in the study of high density clusters.

Both the distance and galactic-latitude criterion are no longer relevant for the definition of a high density cluster, due to our technological advancements, but are historically interesting to note [5]. High density clusters help observational astronomers study the distant universe.

Gravitational lensing is an effect caused by the warping of light as it passes a high mass concentration in the foreground. The gravitational lensing used in this project is the warping of the light from distant galaxies around massive, high density galaxy clusters, defined above. Figure 1.2 is an example of strong gravitational lensing from the ABELL370 cluster. The light from the galaxy at the bottom of the image is very clearly elongated, creating a tail and deserving the nickname "The Dragon". The figure is taken from the cluster ABELL370. Gravitational lensing not only has an effect on the shape of the light; it can create multiple images of the same background source and it can magnify the observed flux of the source as well. The magnification caused by gravitational lensing will be evaluated in section Chapter 2.

There are two types of gravitational lensing: strong and weak. Strong lensing results in the giant arcs, as shown in 1.2. The effects of weak lensing lead to sources only being distorted by a few percent. Both types of lensing are difficult, but possible, to correct in order to obtain accurate information from the observations.

1.3 High Redshift Galaxies

Redshift (z) is a means of describing the receding velocity of a galaxy, due to an expanding Universe. Because light travels at a finite speed, the larger the redshift, the

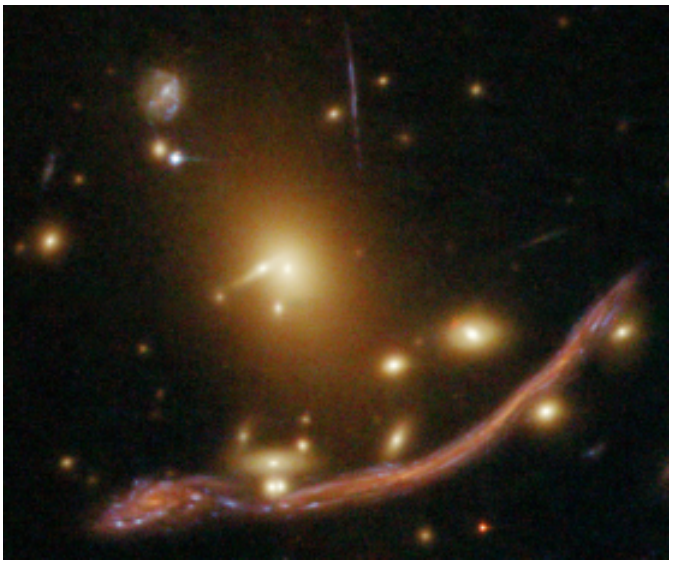

FIGURE 1.2: An example of gravitational lensing as as shown in [1]. The image shoes an observed source lensed by ABELL370 and was obtained prior to the *HFF* campaign. This lensed source is sometimes referred to as 'The Dragon'.

farther back in cosmic time we are probing. Studying high-z galaxies is a way to probe a young Universe. Thus, galaxy evolution can be studied by studying galaxies at different redshift epochs. Some of the farthest galaxies observed today go out to beyond z∼6, or about 10% of the current age of the Universe.

The ideal means of obtaining the redshift of a galaxy is through its spectrum, known as the spectroscopic redshift. This is done by observing the galaxy over a given wavelength range and observing the shifts in known spectral lines when compared to laboratory positions and is given by

$$z = \frac{\lambda_{obs}}{\lambda_{rest}} - 1 \tag{1.2}$$

As sources become fainter at higher redshifts, it becomes increasingly more difficult to obtain the spectrum. Thus, one can find the photometric redshift of a galaxy instead.

The photometric redshift is obtained by measuring the flux of a source at a small number of wavelengths and using these measurements to model a spectral energy distribution (SED). SEDs show trends in the spectrum and can exhibit important features such as the 4000Åbreak, which informs us about internal characteristics of the galaxy, such as stellar population. More specifically, the observed fluxes of the source are compared to models to identify the broad features in the observed SEDs (e.g., Lyman break, Balmer break, etc.). From this comparison, a probability distribution function (PDF) of the redshift of the source is created, based on the fitting of the observed SED. Photometric

redshifts are less reliable than spectroscopic redshifts; one must account for the errors associated with a photometric redshift for any study, while there are practically no errors for the spectroscopic redshift.

Obtaining the full picture of galaxy formation, as mentioned earlier, is to measure the properties of galaxies at different redshifts, and piecing the findings together into one coherent cosmic story. However, because it is harder to observe the far, faint objects, there is an inherent bias in any galactic evolution sample towards high mass objects. Therefore, when attempting to answer the question of how galaxies form and change over cosmological time, we must remember that we are only obtaining part of the story, as we do not yet have the technology to find the oldest, faintest galaxies. Hopefully, when the James Webb Space Telescope launches in 2020, it will be able to detect these objects and we will be able to construct a more comprehensive and complete picture of galaxy formation and evolution across the entire cosmic history.

1.4 Outline

In this thesis, I will probe some of the farthest observed galaxies. The first approach I will take in Chapter 2 is combining the power of the *Hubble Space Telescope* and gravitational lensing in the *Hubble Frontier Fields* campaign. In this chapter, I will evaluate the magnification factors, μ, on all sources observed throughout the campaign. The work presented in Chapter 2 is publicly available and has been published as a part of the HFF-DeepSpace program (PI: Marchesini). I will briefly discuss the program and the data used to derive the magnification factors. Finally, I will provide examples for why these magnification factors are important and need to be accounted for when evaluating lensed sources.

Following, in Chapter 3, I will use data from the UltraVISTA catalogs to study high mass ($\geq 10^{11} M_*/M_\odot$) galaxies between $2 \leq z \leq 6$. The work produced in this chapter will evaluate the distribution of galaxies types (quiescent, dusty star forming, or non-dusty star forming), their spectral energy distributions (SEDs), and will further classify them by noting if these objects have been identified in the X-ray, the radio, or are obscured active galactic nuclei (AGN) as following the methods of [6].

Chapter 2

Hubble Space Telescope Frontier Fields Magnification Calculations

2.1 *HST* Frontier Fields

The *HST* Frontier Fields (*HFF*) campaign combines the power of the Hubble Space Telescope and gravitational lensing, a phenomenon described in Section 1.2, to peer deeper into the distant universe than ever before. The six *HFF* clusters (MACS0416, MACS0717, MACS1149, ABELL1063, ABELL2744, ABELL370) were observed starting in October 2013 until September 2016, with two fields being observed every year. The images produced from the campaign revealed distant galaxies from 10-100 times fainter than previously observed and gave the scientific community the first glimpse of what the James Webb Space Telescope (JWST) will observe when it launches in early 2020 [7].

The catalogs of the six *Hubble* Frontier Fields adopted in my work were constructed by the HFF-DeepSpace program (PI: Marchesini, [8]). The multi-wavelength photometric catalogs include the photometry from the *HFF* images, as well as from the Spitzer Space Telescope images with IRAC 3.6 and 4.5 μm, from the ultra-deep K_s-band (2.2 μm) images from the Keck and VLT telescopes and from deep UV *HST* images. The catalog construction is detailed in Shipley et al. (2018). Briefly, the data were processed in the following way:

1. **Data Reduction:** The latest versions of the *HFF* images were downloaded. Images were run through either the *HFF* or *CLASH* data pipelines for initial correction. All major artifacts were removed and all images were aligned to the same grid based on previous standard *HST* catalogs. A background subtraction was

performed on all science images using a Gaussian interpolation to smooth out the images and remove sky background. Images were cleaned of cosmic rays as well.

2. **"Brightest" Cluster Galaxy (bCG) Modeling:** The *HFF* pointings are centered on massive galaxy clusters with z $\sim$ 0.3-0.5. These clusters, while having the advantage of providing enormous lensing power, have the disadvantage of containing some of the most massive, brightest, and extended galaxies, as well as very bright and extended intra-cluster light (ICL). ICL is the light provided by stars that have been stripped from galaxy cluster members; in the most massive clusters, it constitutes a significant fraction of the total stellar light. In order to be able to take advantage of the full depth of the *HFF* images and detect the most distant and faintest sources, we must first subtract the light from the brightest galaxies in the cluster and the ICL. The initial round of removals was completed using SExtractor[1] with an aggressive background subtraction to identify the centers of the bCGs. The code written to model a bCG was created specifically for elliptical galaxies which represent the majority of the bCGs in clusters of galaxies and thus had some shortcomings when handling spirals.

3. **Source Detection:** After completing the previous two steps, source detection was performed from the $F814W$, $F105W$, $F125W$, $F140W$, and $F160W$ bands using SExtractor and combined to create the detection image. The images are point-spread function (PSF) matched to the $F160W$ band. A PSF was created for each image by stacking unsaturated, isolated stars and, after checking sources by-eye, those which were confirmed to be stars were masked. Estimated fluxes for each band in each field was obtained from SExtractor.

4. **Photometry:** SExtractor was run for each *HST* band. The total flux from the $F160W$ band was determined, when available. If the $F160W$ band was unavailable, the total flux from the $F814W$ band was used. MOPHONGO was used to perform photometry of longer wavelength bands (K_s and *Spitzer*), as it is better equipt to handle low-resolution photometry.

5. **Catalog Construction:** Flags to identify poor quality of the data were input into the catalogs. The images were checked for completeness, as dependent on the different positions and magnitudes of the *HFF* clusters.

More information on the initial handling of the data can be found in [8].

[1]SExtractor is a piece of software that optimally "detects, deblends, measures, and classifies" sources from images [9]. It is able to identify and catalogue multiple astronomical sources in one image. The code can be downloaded here: https://www.astromatic.net/software/sextractor

Due to gravitational lensing, background sources observed have been magnified. The purpose of this chapter is to calculate the magnification values, μ, for all objects observed by each of the 6 HFF clusters. I will describe the methodology of calculating μ followed by an analysis of the results. I adopted a ΛCDM cosmology with $\Omega_M = 0.3$, $\Omega_\Lambda = 0.7$, and $H_0 = 70$ km s^{-1} Mpc^{-1}.

2.2 Methods

2.2.1 Deriving μ

Publicly available lensing models were used to derive magnification values for all sources in the *HFF* clusters.[2] This does not include the available parallel fields. Many independent collaborations have contributed to the creation of different lensing maps for each cluster field (CATS - P.I. Ebeling [2]; Sharon - [10]; Caminha - [11]; Keeton - P.I. Keeton & GLAFIC - [12], [13]; Zitrin LTM & NFW - [14]; Williams - P.I. Williams [15]; Bradac - [16]; Merten - [17]). Each group provided maps for the mass surface-density (κ) and shear (γ).

Briefly, the κ models identified members of the galaxy cluster as created by the individual teams. The γ models are based on the κ models and describe the amount of light distortion as caused by individual members of the galaxy cluster and predominantly by the dark matter mass of the cluster. An example of the FITS files created for each model can be seen in Figure 2.1. Figure 2.1 are the κ (left) and γ (right) for MACS0416 created by CATS [2].

For each source in the catalog, I assigned the κ and γ to the right ascension (RA) and declination (Dec) to the corresponding pixel in the shear and mass maps. The magnification was then derived as

$$\mu = [(1 - \kappa_{scaled})^2 - \gamma_{scaled}^2]^{-1} \tag{2.1}$$

where $\kappa_{scaled} = \kappa \times \frac{D_{LS}}{D_S}$ and $\gamma_{scaled} = \gamma \times \frac{D_{LS}}{D_S}$ [1]. D_{LS} is the distance from the lens to the source and D_S is the distance from the observer (HST) to the source, see Figure 2.2. The distances were derived using the following angular-diameter distance calculation

$$D_A(z_1, z_2) = \frac{c}{1+z_2} \int_{z_1}^{z_2} \frac{dz'}{H(z')} = D_A(0, z_2) - \frac{1+z_1}{1+z_2} D_A(0, z_1) \tag{2.2}$$

[2] https://archive.stsci.edu/prepds/frontier/lensmodels/

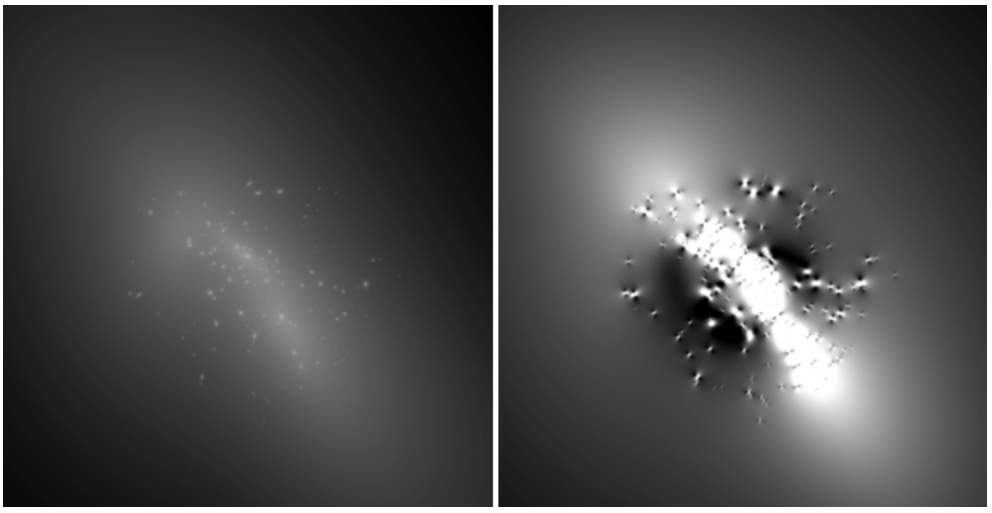

FIGURE 2.1: An example of the "best" model maps from CATS. The left model is the mass surface-density map (κ) and shows the cluster mass distribution as well as the gas mass as determined by CATS [2]; the right model is the shear (γ) and shows the amount of distortion caused by members of the galaxy cluster. The galaxy cluster in this model is MASCS0416 [2].

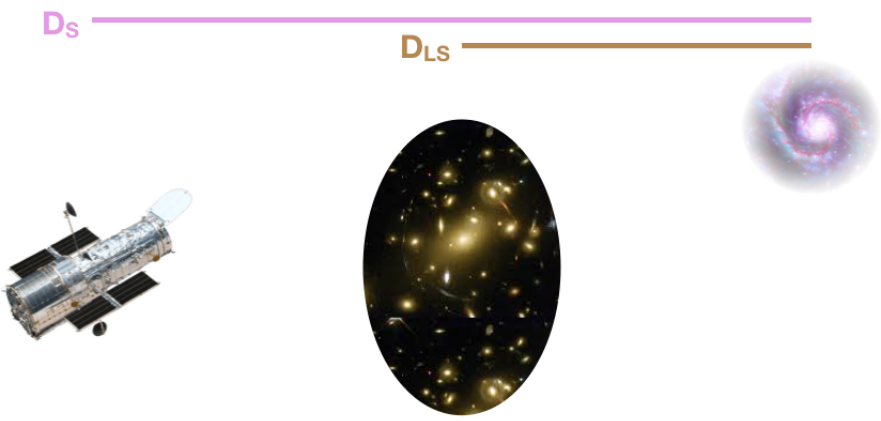

FIGURE 2.2: The distances D_S and D_{LS}, as measured angular diameter distances, are necessary for scaling κ, the mass-surface density, and γ, the shear to obtain accurate magnification factors.

where, for a flat universe, the Hubble parameter varies with

$$H(z) = H_0\sqrt{\Omega_m(1+z)^3 + \Omega_\Lambda} \tag{2.3}$$

The reason why the κ and γ parameters scale as a function of redshift is because if a background source is closer to the lensing cluster, the angle at which the light is bent remains constant. In order to account for this for background sources at all redshifts, the image deflection is scaled by the distance ratio, D_{LS}/D_S [1].

Cluster	Redshift (z_L)
abell1063	0.348
abell2744	0.308
abell370	0.375
macs0416	0.396
macs0717	0.545
macs1149	0.543

TABLE 2.1: Table of the six *HFF* clusters and their associated redshifts (z_L).

Using the angular-diameter distance equation, I find the distance from the observer to the source using $D_S = D_A(0, z_S)$, where z_S is the redshift of the source, and $D_{LS} = D_A(z_L, z_S)$, where z_L is the redshift of the lens [1]. The redshift of the lenses are found in Table 2.1.

For each cluster, I derived the lensing magnifications for sources in the HFF-DeepSpace catalogs that used an estimated photometric redshift, when a spectroscopic redshift was unavailable. This work resulted in two lensing magnification catalogs which were part of the public data release of the HFF-DeepSpace collaboration.[3] Both catalogs included columns for lensing magnification of the sources for different group's derived model. One catalog lists errors of magnification factors derived from the model uncertainties and the other lists the errors of the magnification factors derived from photometric redshift uncertainties. The process is further discussed in the following section.

2.2.2 Statistical Analysis

I analyzed the error on the magnification factor derived from model uncertainties. Each group made available "best" γ and κ maps as well as anywhere from 30-200 additional maps. The "best" maps were deemed the best by the group and were used to calculate the best lensing magnification for each object in all of the fields. The additional maps, whose numbers varied from group to group, were used to derive the associated error.

For every field, and every model associated with that field, a μ was calculated for the additional maps provided by the groups. The mean, median, lower 68th percentile, and the upper 68th percentile were calculated using the derived magnifications. I would like to clarify that not every groups' maps included all of the sources in our own catalogs. Thus, if a source did not fall within the area of the lensing map for a given group, the source is flagged with a -50 value.

[3] http://cosmos.phy.tufts.edu/ danilo/HFF/Home.html

In each cluster, I derive the lensing magnifications for sources in our catalogs that have an available spectroscopic or photometric redshift. For those sources without spectroscopic redshifts, statistical analysis on the probability distribution function (PDF) of the photometric redshift was conducted. The PDF was derived from the publicly available code, EAZY.[4] I chose 300 photometric redshifts within the PDF at random and calculated μ using the "best" model for all redshifts. Again, the mean, median, lower 68th and upper 68th percentiles were calculated and included in the catalog on redshift error. Objects with available spectroscopic redshifts had a magnification and associated errors of 1 within the catalog.

Different flags were used to populate the catalogs if there was something inadequate about the source or the model. The flags are noted as:

1. If a source did not have a spectroscopic or estimated photometric redshift, μ and associated errors have values of -99.
2. If a source's RA and Dec were not present on the model map (i.e. the model was too small), μ and associated errors have values of -50.
3. If a source had a use_phot = 0, μ and associated errors have values of -1.
4. If a source has a redshift less than the cluster redshift ($z_S < z_L$), μ has a value of 1.

2.3 Results

The resulting magnification catalogs are best displayed in segmentation maps. The segmentation map is populated with the derived lensing magnifications specific to each source. This is done by matching the source ID in the map to the best magnification derived from a given model. The subfigures are labeled with the name of which group's map was used. The darkest sources are the most heavily lensed objects, closest to objects within the lensing cluster map, and the lightest are the least lensed (see color bar for a more detailed breakdown of μ values). Figure 2.3, shows the differences between the cluster fields all using the same CATS maps. This model was deemed the best due to large coverage and the least amount of overlapping sources with the lensing cluster. Figures 2.4, 2.6, 2.7, 2.8, 2.9, and 2.10 all show the differences between the lensing models for each group of the appropriate cluster. In these figures, it is important to take notice of the differing map sizes from model to model and that some of the models are not available for every cluster.

[4] https://github.com/gbrammer/eazy-photoz

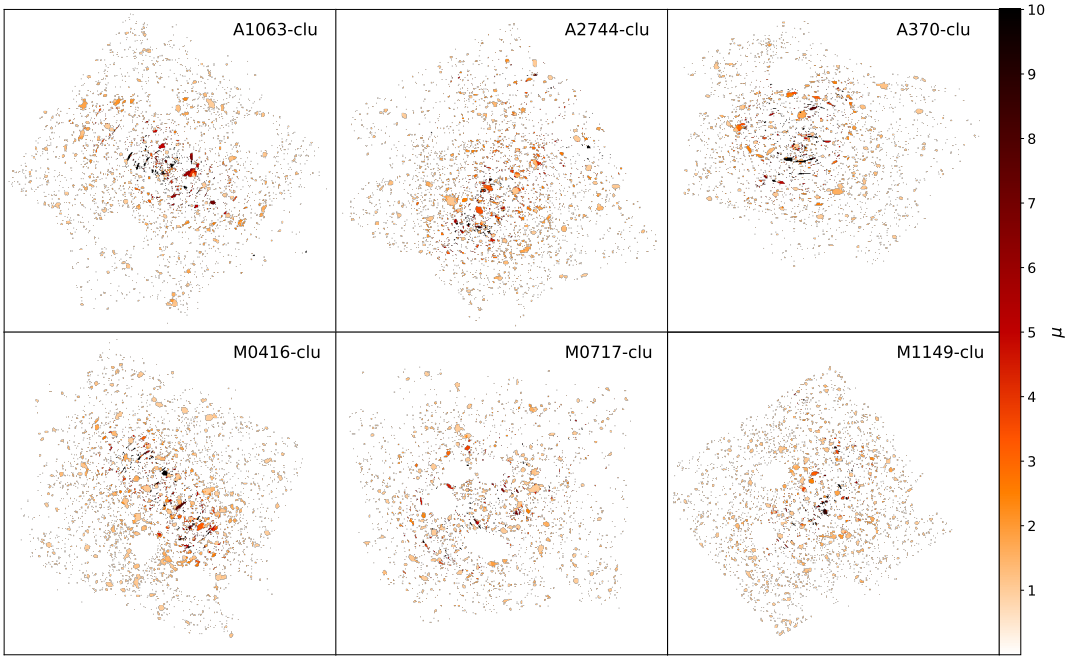

FIGURE 2.3: The magnification factors from the lensing model CATS for all six clusters. The segmentation maps produced are populated with the derived lensing magnifications specific to each cluster using the "best" CATS κ and γ maps. The sources are color coded by lightly lensed (light sources) to heavily lensed (dark sources); see the associated color bar for more specific magnification breakdown.

In addition to the populated segmentation maps, the relationship between mass of the galaxy (M_*) and the lensing magnification corrected mass of the galaxy (M_*/μ) can be seen in Figure 2.11. As demonstrated, when taking the lensing magnification into account, the mass of source decreases. In many cases as well, the higher the redshift of the object, the more the mass needs to be corrected, i.e. it has a higher μ factor. Sources with a $\mu = 1$ were not included in this figure as these sources had redshifts smaller than the redshift of the cluster and were not affected by gravitational lensing.

2.4 Concluding Remarks

The *HFF* campaign, using both the *Hubble* Space Telescope and gravitational lensing caused by massive galaxy clusters allows us to probe into a galactic regime which would otherwise be difficult to study. Because background sources are magnified, we are able to observe and study the low stellar mass and low luminosity galaxies which would otherwise be out of our reach. As shown in Figure 2.11, thanks to the lensing magnification, we are able to probe dwarf galaxies with de-lensed stellar masses as low as $Log_{10}M_*/M_\odot \sim 6$ at z $>$ 5!

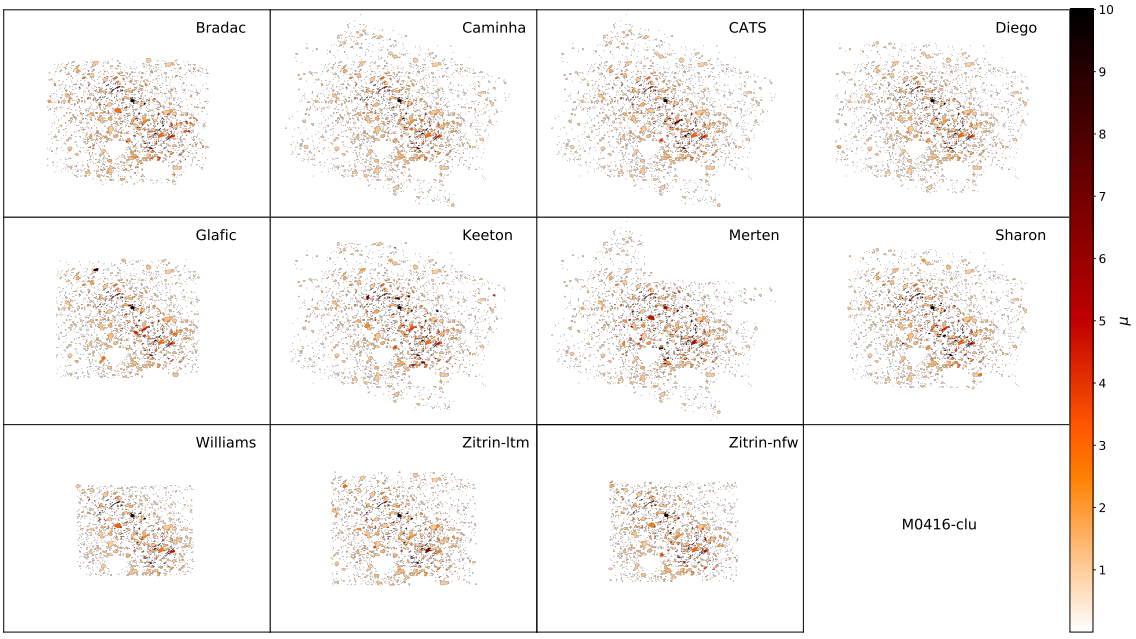

FIGURE 2.4: The magnification factors from the lensing models for each group of the MACS0416 cluster. The segmentation maps produced as part of the collaboration are populated with the derived lensing magnifications specific to each source for the various group's lensing model (labeled in panel). The sources are color coded by lightly lensed (light sources) to heavily lensed (dark sources); see the associated color bar for more specific magnification breakdown. This figure clearly demonstrates the varying coverage areas for each group's lensing model, as mentioned in the text. All other clusters are below.

In order to take full advantage of the unmatched depth of the *HFF* images to study the galaxy population in the first billion years of cosmic history, the properties of the galaxies (e.g. stellar mass, luminosity, and star-formation rates) must be corrected for the lensing magnification of the foreground clusters of galaxies. As part of the HFF-DeepSpace program, I led the derivation of the lensing magnification factors of all sources detected in the *HFF* images, and I constructed catalogs of lensing magnifications and associated random and systematic uncertainties. The catalogs of the HFF-DeepSpace program, including the lensing magnification catalogs, have been publicly released to the astronomy community in order to maximize the return of the enormous investment of the *Hubble* Space Telescope. The products of the HFF-DeepSpace program can be found here: http://cosmos.phy.tufts.edu/~danilo/HFF/Home.html.

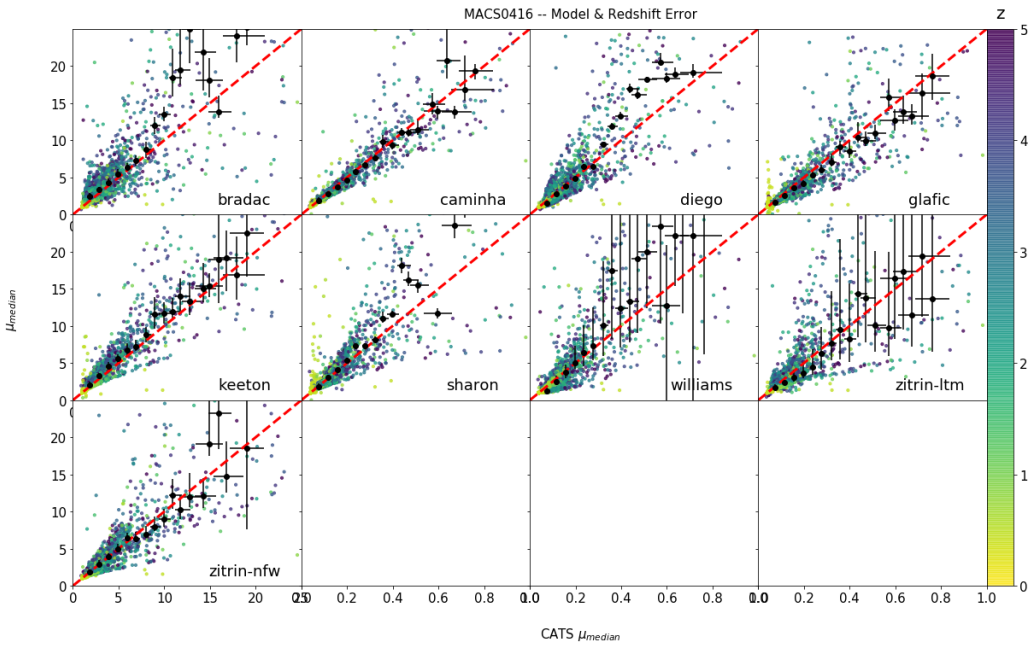

FIGURE 2.5: Models used to calculate the magnification factors were created by individual teams. This figure demonstrates the varying results as compared to the CATS model, which was deemed the best by our team, for MACS0416. The dashed red line represents a one-to-one relation. The black points represent the median binned magnification factors and the error bars represent the 15th and 85th percentile values.

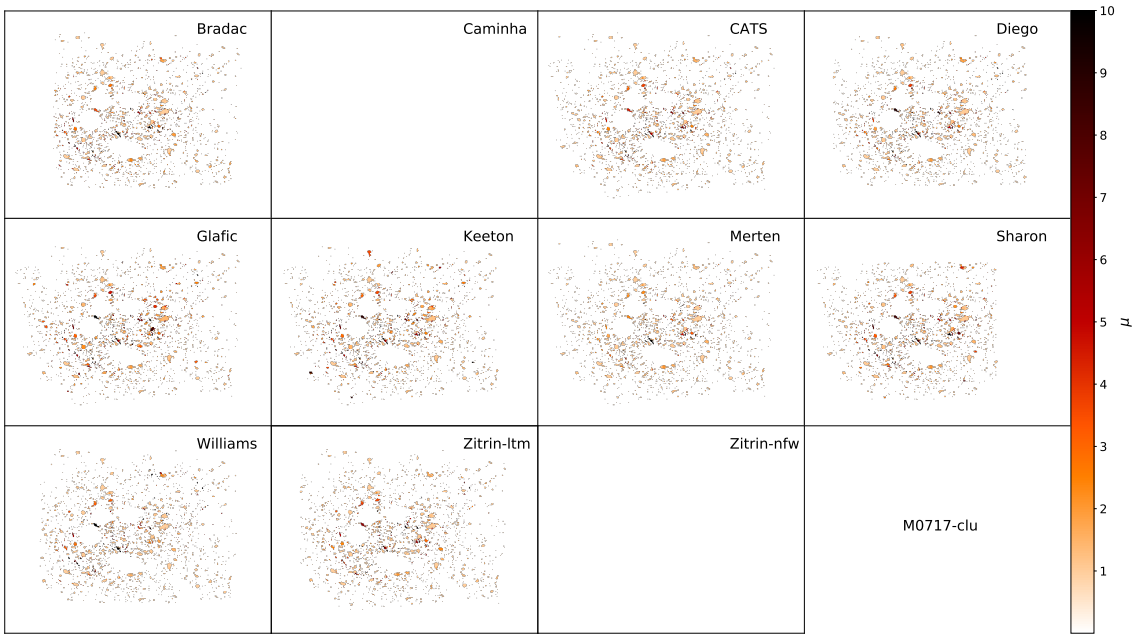

FIGURE 2.6: The magnification factors from the lensing models for each group of the MACS0717 cluster. Empty figures means the model was not available for this cluster.

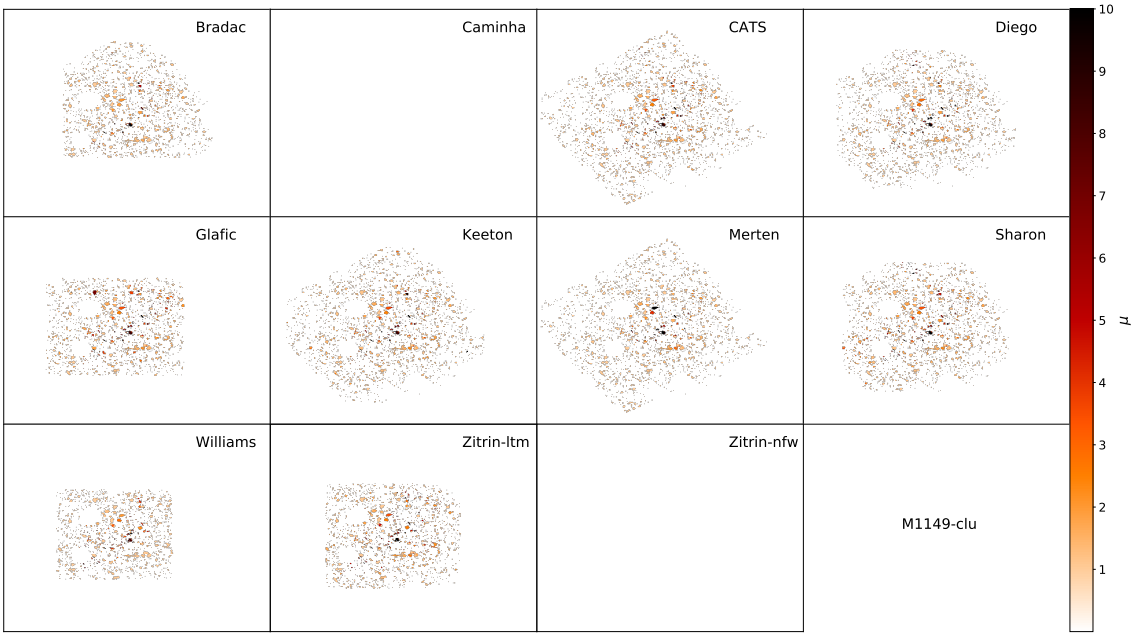

FIGURE 2.7: The magnification factors from the lensing models for each group of the MACS1149 cluster. Empty figures means the model was not available for this cluster.

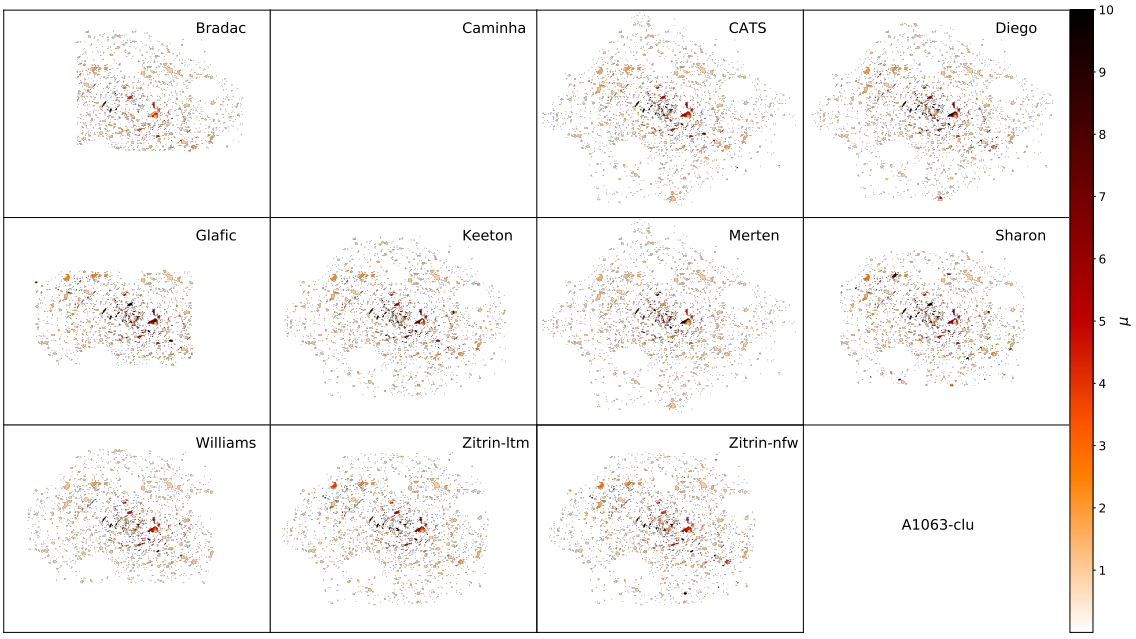

FIGURE 2.8: The magnification factors from the lensing models for each group of the ABELL1063 cluster. Empty figures means the model was not available for this cluster.

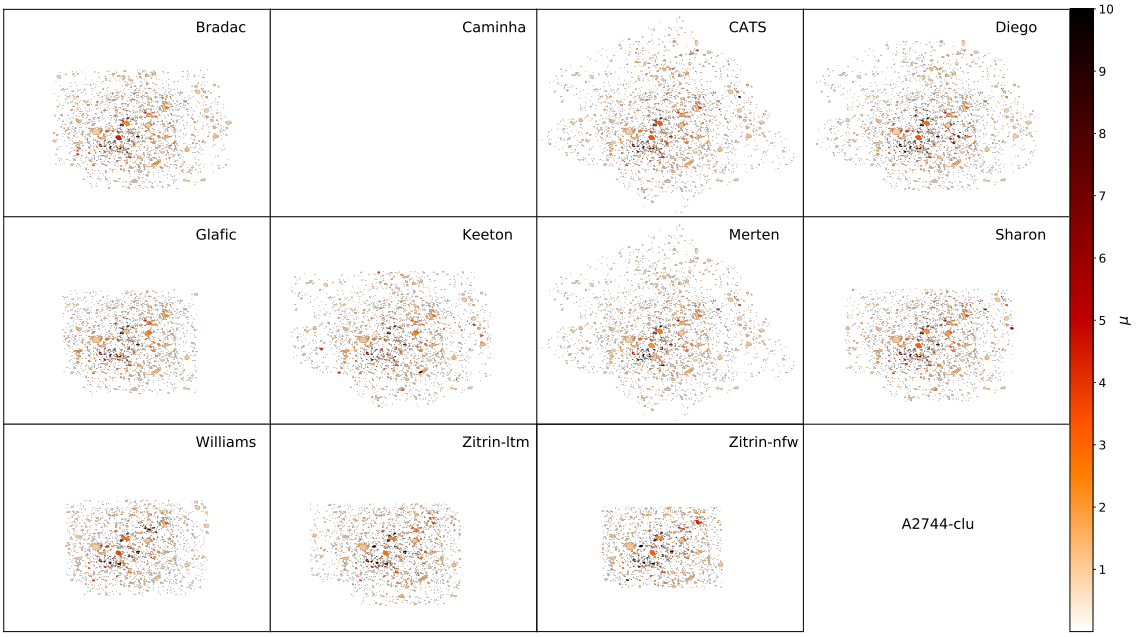

FIGURE 2.9: The magnification factors from the lensing models for each group of the ABELL2744 cluster. Empty figures means the model was not available for this cluster.

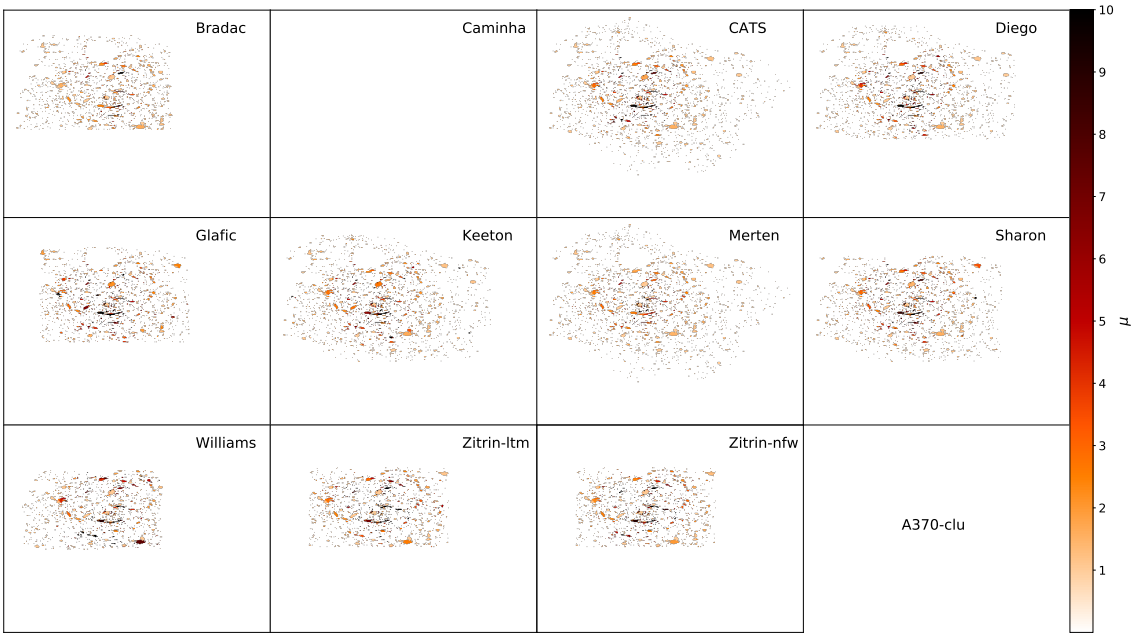

FIGURE 2.10: The magnification factors from the lensing models for each group of the ABELL370 cluster. Empty figures means the model was not available for this cluster.

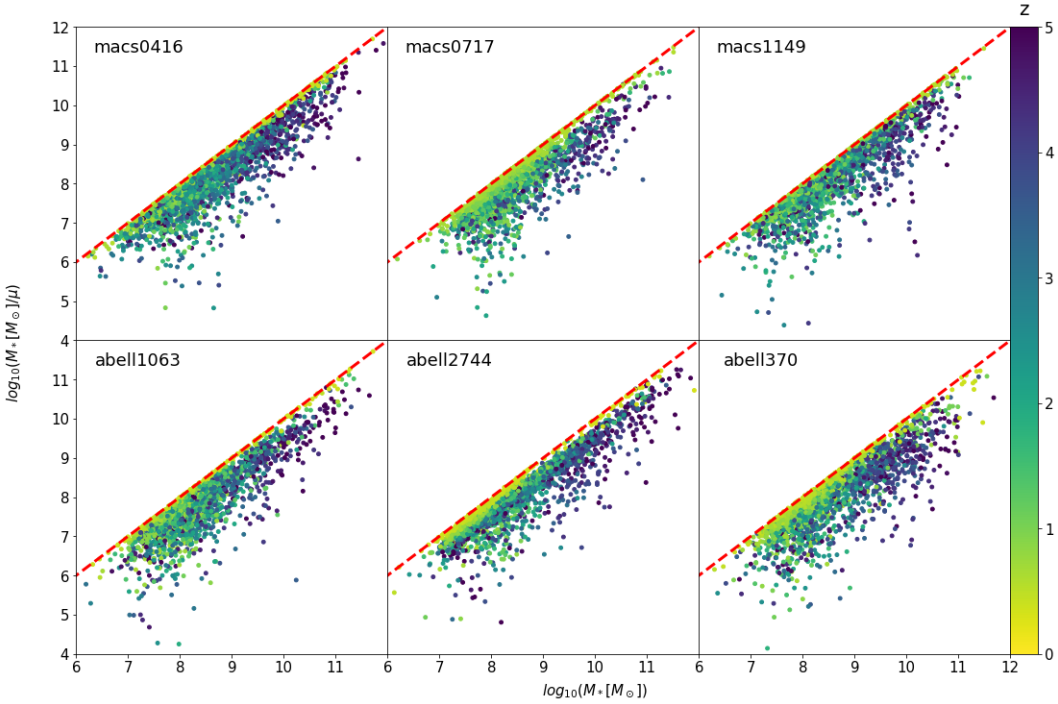

FIGURE 2.11: A comparison of source mass M_* vs corrected source mass M_*/μ using the best μ from the CATS model and color coded by the redshift of the source (see color bar). The one-to-one relation is plotted as a dashed red line.

Chapter 3

High Mass Galaxies in the UltraVISTA Catalogs

3.1 The UltraVISTA Catalogs

The UltraVISTA survey is an ultra deep, near-infrared survey with the VISTA (Visible and Infrared Survey Telescope for Astronomy) telescope located in Chile. The VISTA telescope covers the Z, Y, J, H, K_s bands, from $\sim$ 0.9 - 2.2 microns as well as the narrow band at 1.18 μm [18]. Due to its unique combination of wide surveyed area and depth, allowing for the detection of very faint distant objects, the UltraVISTA survey represents a significant improvement with respect to any other near-infrared surveys [19].

The UltraVISTA survey covers 1.62deg^2 in the COSMOS field, which contains an impressive wealth of multi-wavelength data. COSMOS includes coverage in the X-ray (*XMM - Newton; Chandra*), the UV (*GALEX* satellite), several broad-band and medium-band optical (CFHT & Subaru), mid-infrared (*Spitzer*), sub-millimeter (*Herschel*), millimeter (AzTEC; MAMBO), and in the radio (VLA). Having such a complete wavelength coverage makes studying distant galaxies highly attractive and interesting [20].

The version of the UltraVISTA catalog used to perform this study is v3.3 (Muzzin et al. 2018; in prep.) has not yet been publicly released.

3.2 Methods

In order to select a clean sample of galaxies, sources in the UltraVISTA catalogs were filtered out by the following parameters: contamination = 0, nan_contam < 3, star = 0,

$M_K^{AB} < 25$, and use = 1. Once all cuts were applied to the data, 781 high-mass objects ($log(M_*/M_\odot)$ >11.0) at $2 \leq z \leq 6$ were identified.

The sample was divided into one of the following categories: quiescent (Q), non-dusty star-forming (ndSF), and dusty star-forming (dSF) based on their $U - V$ and $V - J$ colors using the definition from [3]. Star-forming (both dusty and non-dusty) galaxies satisfy:

$$(U - V) < 1.3 \text{ for } (V - J) < 0.75 \tag{3.1}$$

and

$$(U - V) < 0.8(V - J) + 0.7 \text{ for } (V - J) \geq 0.75 \tag{3.2}$$

This condition is shown in Figures 3.3 and 3.4 as the solid black line. In order to further characterize the population, dSF galaxies are identified within the population of star-forming galaxies using:

$$(U - V) < 1.43(V - J) - 0.36 \tag{3.3}$$

and is represented in Figures 3.3 and 3.4 as the dashed black line. Additionally, the sections of the figure are labeled accordingly. These relations were taken from [3], but can also be found in several other published articles ([21], [22]).

The next step was to check the SEDs and stamp figures for the galaxies in our sample for any additional contamination. The observed SEDs (fluxes and associated errors as a function of wavelength) for the sample were plotted along with the best-fit models of the SEDs output by EAZY and FAST. EAZY is a software package used to model the observed SED to derive photometric redshifts and rest-frame colors, whereas FAST is a software used to model the observed SED to derive stellar population properties of the modeled galaxy, e.g. stellar mass, star-formation rate, and dust extinction. EAZY also outputs the PDF of the redshift for each object, which was plotted along with the best-fit photometric redshift, lower 68th and upper 68th percentile ranges, and the spectroscopic redshift when available. Stamp images in the following bands were also included: HST F814W ($\lambda \sim 0.8$ micron), NB118 ($\lambda \sim 1.19$ micron), HST F160W ($\lambda \sim 1.6$ micron), K_s ($\lambda \sim 2.15$ micron),Y ($\lambda \sim 1.02$ micron), J ($\lambda \sim 1.25$ micron), and H ($\lambda \sim 1.64$ micron).

Additionally, sources were cross checked with the radio catalog provided by [23] which were observed via the VLA and the x-ray catalog provided by [24] which were observed using the Chandra X-ray Observatory. The position of the sources in the UltraVISTA catalogs were compared with the position of sources in the two additional catalogs.

Sources in the UltraVISTA whose distance was ≤ 1 arcsecond away from a object in the radio catalog were identified as radio sources. Sources in the UltraVISTA whose distance was ≤ 0.3 arcseconds away from a object in the X-ray catalog were identified as X-ray sources.

Furthermore, sources were evaluated as potential obscured active galactic nuclei (AGN). This was done by studying the IRAC data from all 4 channels: 3.6, 4.5, 5.8, and 8.0 μm following the methods of [6]. Sources whose results met the following criteria were identified as potential AGN:

$$\begin{aligned} x \geq 0.08 \wedge y \geq 0.15 \wedge y \geq (1.21 \times x) - 0.27 \wedge y \leq (1.12 \times x) + 0.27 \\ \wedge f_{4.5\mu m} > f_{3.6\mu m} \wedge f_{5.8\mu m} > f_{4.5\mu m} \wedge f_{8.0\mu m} > f_{5.8\mu m} \end{aligned} \tag{3.4}$$

where

$$x = log_{10} \frac{f_{5.8\mu m}}{f_{3.6\mu m}} \tag{3.5}$$

and

$$y = log_{10} \frac{f_{8.0\mu m}}{f_{4.5\mu m}} \tag{3.6}$$

as taken from [6]. Figure 3.1 provides an example of such a figure. Additionally, several properties of the galaxy were printed as well, including $Log(M_*[M_\odot])$, redshift, the type of galaxy, as determined by the UVJ diagram, and if it was identified in any additional catalogs.

3.3 Results

After applying the appropriate data cuts mentioned in Section 3.2 to the entire catalog and then checking SEDs by-eye for the massive, high-redshift galaxies I wanted to analyze for any additional contamination, a total of 721 massive galaxies between $2 \leq z \leq 6$ remain as our sample. Figure 3.2 shows the total data set, in black, and the sources in the sample used for this analysis, in red.

Figure 3.3 plots the U-V versus V-J colors (UVJ diagram) for each object in the UltraVISTA catalog. The points are colored by the source's redshift. The spectroscopic redshift was used when available, otherwise the photometric redshift was used. The plot is divided into 3 sections: quiescent (Q), dusty star-forming (dSF), and non-dusty star-forming (ndSF) [3]. The points are relatively scattered by redshift, however the

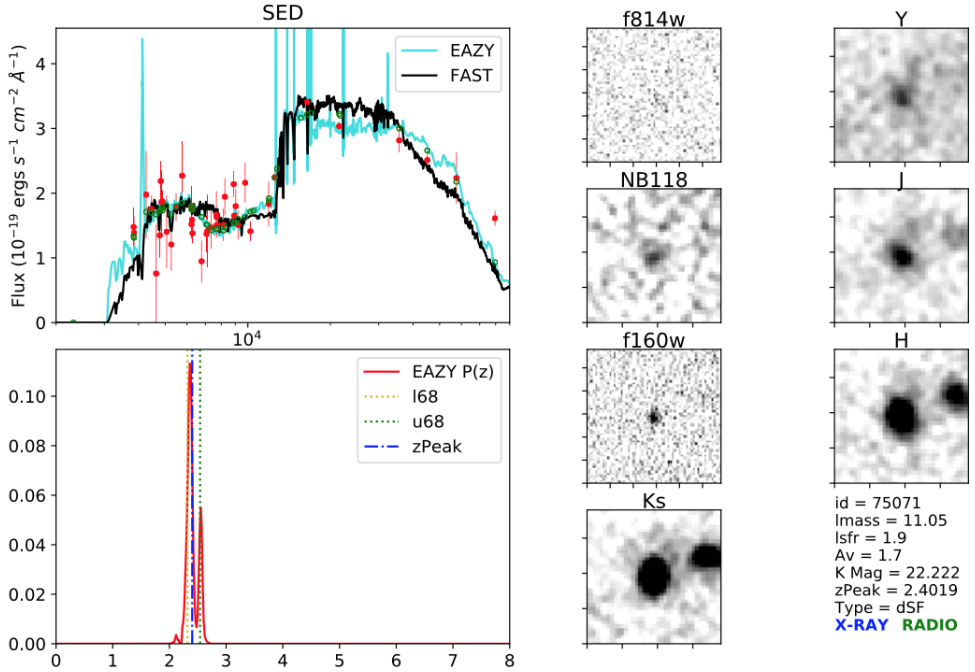

FIGURE 3.1: An example of the plotted SED, P(z), stamp images, characteristics of, and the identifiaction of an x-ray, radio, or AGN for a given source. A figure like this was created for every object in our sample.

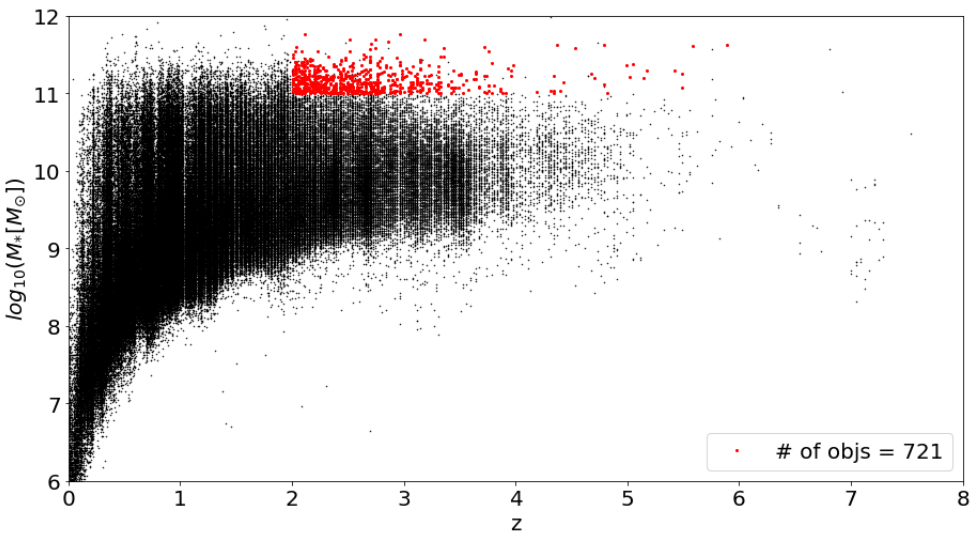

FIGURE 3.2: Sources present in the UltraVISTA catalogs after performing initial cuts. Black points represent every source; red points represent sources which meet the mass cut ($M_* \geq 10^{11} M_\odot$) and the redshift range in question ($2 \leq z \leq 6$).

highest redshift sources predominantly lie in the quiescent region of the plot. This sample provides us with a fair number of each type of galaxy for further analysis.

Again, I further divided the UVJ diagram by redshift and colored the points by the

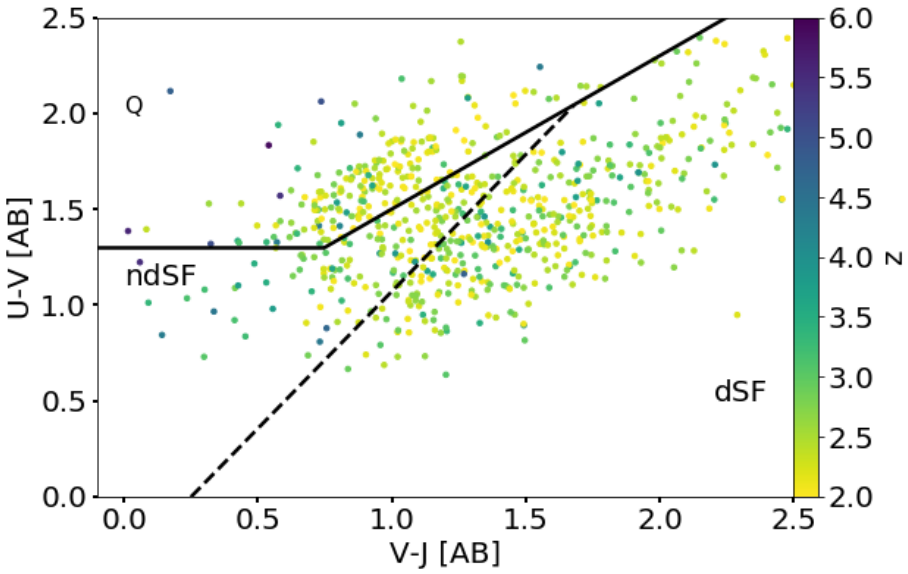

FIGURE 3.3: The divisions between quiescent, star-forming, and dusty star-forming galaxies in the UVJ diagram was taken from [3].

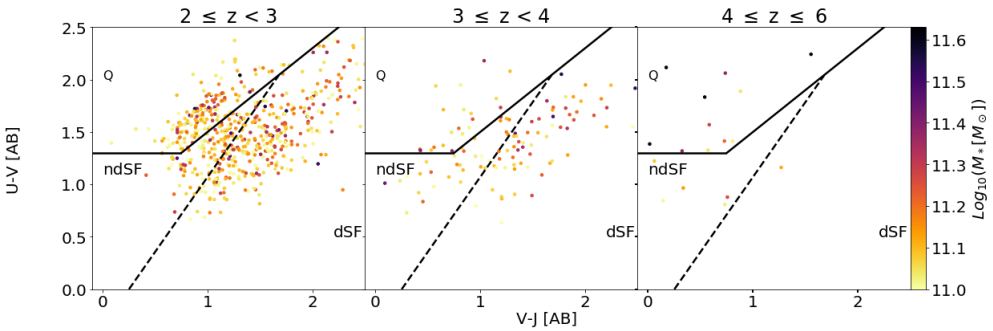

FIGURE 3.4: The divisions between quiescent, star-forming, and dusty star-forming galaxies in the UVJ diagram was taken from [3]

given mass of the galaxy. There are approximately 582 objects at $2 \leq z < 3$, 115 objects at $3 \leq z < 4$, and 24 objects at $4 \leq z < 6$.

3.4 Concluding Remarks

After sorting galaxies by color and ensuring the sources were good via visual inspection, their SEDs, taken from FAST, were stacked for further analysis, Figure 3.5. The 100 evenly spaced bins were created between 1-3 μm. The median flux values for every bin was taken, to obtain the solid curve seen in Figure 3.5 and the shaded region represents the 15th to the 85th percentiles per bin. Blue represents the galaxy population from $2 \leq z < 3$; red represents $3 \leq z < 4$; green represents $4 \leq z \leq 6$. These colors represent

the population in Figure 3.5, Figure 3.6, and Figure 3.7. The small, gray points in Figure 3.5 represent the observed flux extracted from EAZY. In Figure 3.5, we note the decreasing strength of the 4000Åbreak as the redshift increasing, suggesting an younger, star-forming population. This figure allows us to view the overall trend within each redshift bin.

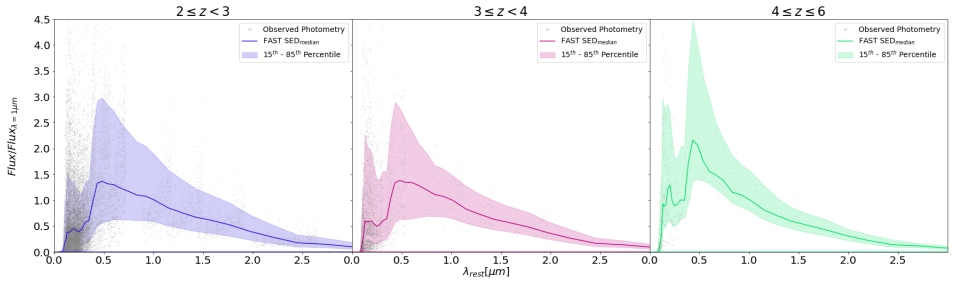

FIGURE 3.5: Binned, average SED for all sources in each redshift bin, where blue represents $2 \leq z < 3$, red represents $3 \leq z < 4$, and green represents $4 \leq z \leq 6$. The shades region represents the 15th to the 85th percentiles per bin. The small, gray points represent the observed flux extracted from EAZY. The flux is normalized to the flux at $\lambda = 1\mu m$.

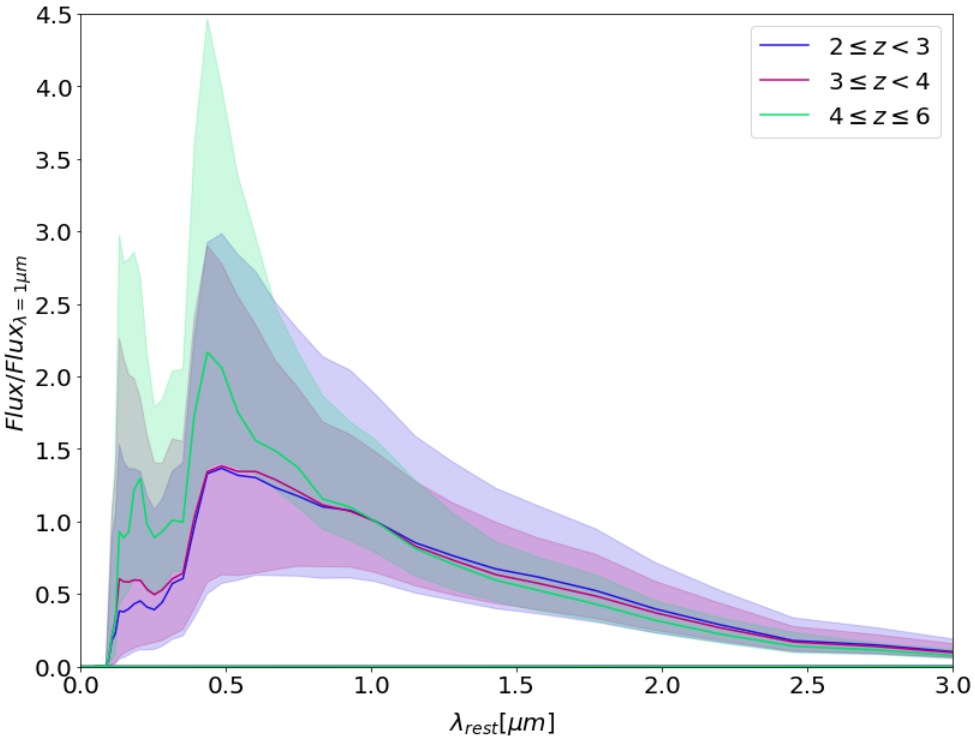

FIGURE 3.6: The same SED binning applied to Figure 3.5, except over-plotted to further note the decreasing strength of the 4000Åbreak as the redshift of the galaxy population increases. The flux is normalized to the flux at $\lambda = 1\mu m$.

The trend is better seen in Figure 3.5, which is the same as Figure 3.5, but with each redshift bin over plotted. The galaxy population between z $\sim$ 4-6 very clearly contains

more quiescent sources and very subtly there is a difference between the z $\sim$ 2-3 and z $\sim$ 3-4 populations, as noted by the slightly stronger 4000Åbreak in the solid blue line. Galaxies are believed to have just started forming at high redshifts and thus the results for z $\sim$ 4-6 are unexpected. It is possible these objects are severely dust obscured and the UVJ color cutoffs for quiescent vs. star-forming galaxies does not apply in this regime. These sources require further investigation.

As the redshift of the sources increases, Figure 3.6, there is a noticeable increase in the averaged flux, normalized to $flux(\lambda = 1\mu m)$. The overall shape for the dusty star-forming galaxies for $2 \leq z < 4$ appear very similar, although the spread is slightly different; this could also be due to the different number of sources per redshift bin. The SEDs per redshift bin can be further broken down into galaxy population activity levels, as identified by the UVJ colors and previously seen in Figure 3.4.

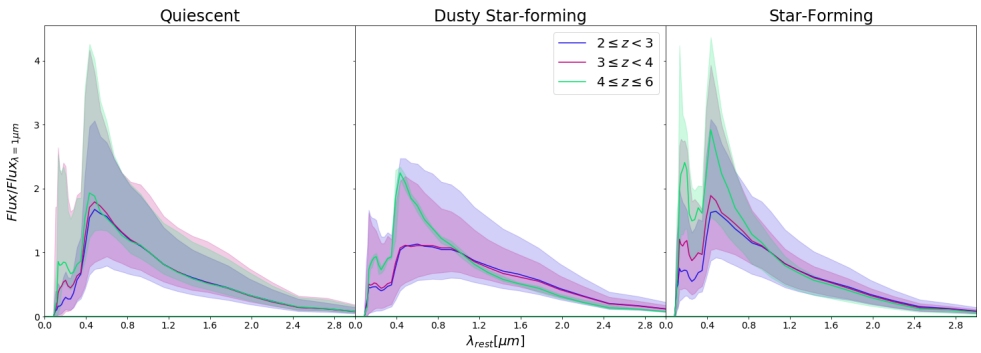

FIGURE 3.7: The same SED binning applied to Figure 3.5, except broken into quiescent (top), dusty star-forming (middle), and non-dusty star-forming (bottom) based on UVJ colors. The flux is normalized to the flux at $\lambda = 1\mu m$.

Starting for the quiescent population (left) in Figure 3.7, one notes the similarity in trends with only the slight difference in strength of the 4000Åbreak, indicating, again, a younger population at lower redshifts. For the dusty star-forming population (middle), the SEDs for the population between z $\sim$ 2-4 is very close to being identical and for the source in z $\sim$ 4-6, we note that the spread of the function is minimal because there was only a single source identified. The same trend identified for the quiescent population can be seen in the non-dusty star-forming population (right).

All three concluding figures suggest that as the redshift of galaxy increases, the increasing strength of the 4000 Åbreak suggests an increase in the age of the population. It is not possible to make any definite claims for dusty star-forming galaxies at z $\sim$ 4-6, because there is only one source identified. However, it may be likely that the UVJ diagram cutoffs for quiescent vs. star-forming sources become inaccurate at higher redshifts, as we would not expect the majority of the population to be quiescent, as identified in this sample.

Ultimately, the study of galaxy formation and evolution requires the use of the James Webb Space Telescope (JWST) in 2020 in order to further probe the properties of the deepest objects in the universe. Through improved technology, we may be able to answer questions such as if the UVJ color diagram limits for quiescent vs. star-forming galaxies change over cosmic time and why dusty star-forming galaxies at z $\sim$ 2-4 show little to no evolution over such a long period of time.

Bibliography

[1] Hubble frontier fields: Strong gravitational lensing primer. October 2013. URL https://archive.stsci.edu/prepds/frontier/lensmodels/webtool/hlsp_frontier_model_lensing_primer.pdf.

[2] Article navigation *Hubble Frontier Fields*: a high-precision strong-lensing analysis of galaxy cluster macsj0416.1-2403 using 200 multiple images. *MNRAS*, 443(2), July 2014. doi: https://doi.org/10.1093/mnras/stu1355.

[3] The evolution of the fractions of quiescent and star-forming galaxies as a function of stellar mass since z = 3: Increasing importance of massive, dusty star-forming galaxies in the early universe. *ApJ*, 827(2), January 2012. URL http://iopscience.iop.org/article/10.3847/2041-8205/827/2/L25/meta.

[4] Mo Houjun et al. *Galaxy Formation and Evolution*. Cambridge University Press, 2010.

[5] The distribution of rich clusters of galaxies. *ApJS*, 211(3), September 1958.

[6] Identifying luminous agn in deep surveys: Revised irac selection criteria. *AJ Letters*, August 2016. URL https://arxiv.org/abs/1201.3899.

[7] Telescope frontier fields. 2016. URL http://www.stsci.edu/hst/campaigns/frontier-fields/.

[8] Hff-deepspace photometric catalogs of the twelve *Hubble* frontier fields, clusters, and parallels: Photometry, photometric redshifts, and stellar masses. *ApJS*, 235 (1), March 2018. URL https://arxiv.org/abs/1801.09734.

[9] The *Chandra* cosmos survey iii. optical and infrared identifiaction of x-ray point sources. *Astronomy & Astrophysics Supplement Series*, 117, June 1996. doi: 10.1051/aas:1996164.

[10] Lens models and magnification maps of the six hubble frontier fields clusters. *ApJ*, 797(1), May 2014. doi: 10.1088/0004-637X/797/1/48.

[11] A refined mass distribution of the cluster macs j0416.12403 from a new large set of spectroscopic multiply lensed sources. *A & A*, 600(1), July 2016. doi: 10.1051/0004-6361/201629297.

[12] The mass distribution of sdss j10044112 revisited. *PASJ*, 62(4), July 2010. doi: https://doi.org/10.1093/pasj/62.4.1017.

[13] Hubble frontier fields first complete cluster data: Faint galaxies at z $\sim$ 5-10 for uv luminosity functions and cosmic reionization. *ApJ*, 799(1), July 2015. doi: 10.1088/0004-637X/799/1/12.

[14] Clash: The enhanced lensing efficiency of the highly elongated merging clusters macs j0416.1-2403. *ApJ*, 762(2), December 2013. URL http://iopscience.iop.org/article/10.1088/2041-8205/762/2/L30/meta.

[15] Clash-vlt: Insights on the mass substructures in the frontier fields cluster macs j0416.1-2403 through accurate strong lens modeling. *ApJ*, 800(1), March 2015. URL http://iopscience.iop.org/article/10.1088/0004-637X/800/1/38/meta.

[16] Focusing cosmic telescopes: Exploring redshift z $\sim$ 5-6 galaxies with the bullet cluster 1e0657-56. *ApJ*, 706, July 2009. doi: 10.1088/0004-637X/706/2/1201.

[17] Creation of cosmic structure in the complex galaxy cluster merger abell 2744. *MNRAS*, 417(1), March 2011. doi: 10.1111/j.1365-2966.2011.19266.x.

[18] Vista: Visible and infrared survey telescope for astronomy. http://www.vista.ac.uk/. Accessed: 2018-04-20.

[19] Ultravista: a new ultra-deep near-infrared survey in cosmos. *A& A*, 544, August 2012. doi: 10.1051/0004-6361/201219507.

[20] A public k_s-selected catalog in the cosmos/ultravista field: Photometry, photometric redshifts and stellar population parameters. *ApJSS*, March 2013. doi: 10.1088/0067-0049/206/1/8.

[21] Galaxy structure as a driver of the star formation sequence slope and scatter. *ApJ Letters*, 811(1), September 2015. doi: 10.1088/2041-8205/811/1/L12.

[22] Uv to ir luminosities and dust attenuation determined from $\sim$ 4000 k-selected galaxies at $1 < z < 3$ in the zfourge survey. *ApJ Letters*, February 2015. doi: 10.3847/2041-8205/818/2/L26.

[23] The vla-cosmos 3ghz large project: Multiwavelength counterparts and the composition of the faint radio population. *A& A*, 602(A2), April 2017. URL https://arxiv.org/abs/1703.09719.

[24] The *Chandra* cosmos survey iii. optical and infrared identifiaction of x-ray point sources. *ApJS*, August 2012. URL https://arxiv.org/abs/1205.5030.